γδ T-cells regulate intestinal response to nutrient sensing

Zuri A. Sullivan[1], **William Khoury-Hanold**[1], **Jaechul Lim**[1], **Chris Smillie**[2], **Moshe Biton**[2,†], **Bernardo S. Reis**[3], **Rachel K. Zwick**[4], **Scott D. Pope**[1,5], **Kavita Israni-Winger**[1], **Roham Parsa**[3], **Naomi H. Philip**[1], **Saleh Rashed**[1], **Noah Palm**[1], **Andrew Wang**[1,6], **Daniel Mucida**[3], **Aviv Regev**[2,7,8], **Ruslan Medzhitov**[1,5,*]

[1]Department of Immunobiology, Yale University School of Medicine, New Haven, CT, USA

[2]Klarman Cell Observatory, Broad Institute, Cambridge, MA, USA

[3]Laboratory of Mucosal Immunology, The Rockefeller University, New York, NY, USA

[4]Program in Craniofacial Biology and Department of Orofacial Sciences, University of California, San Francisco, CA, USA

[5]Howard Hughes Medical Institute, New Haven, CT, USA

[6]Department of Medicine (Rheumatology), Yale University School of Medicine, New Haven, CT, USA

[7]The David H. Koch Institute for Integrative Cancer Research at MIT, Department of Biology, MIT, Cambridge, MA, USA

[8]Howard Hughes Medical Institute, Cambridge, MA, USA

Abstract

A site of direct encounter with the external environment, the intestine must balance barrier defense with nutrient uptake. To investigate how nutrient uptake is regulated in the small intestine, we tested the effect of diets with different macronutrient composition on epithelial gene expression. We found that enzymes and transporters required for carbohydrate digestion and absorption were regulated by carbohydrate availability. Surprisingly, the "on-demand" induction of this machinery required γδ T cells, which regulated this program via the suppression of IL-22 production by type 3 innate lymphoid cells (ILC3s). Nutrient availability altered the tissue localization and transcriptome of γδ T cells, and transcriptional responses to diet involved cellular remodeling of the epithelial compartment. This work thus identified a role for γδ T cells in nutrient sensing.

One Sentence Summary

γδ T-cells regulate transcriptional response to diet in the intestinal epithelium.

Introduction

Animal diets range in diversity. Specialists rely on a restricted set of food sources, whereas generalists, like humans and other omnivores, derive nutrition from diverse foods (1). For specialists, fixed morphologic adaptations in the organization of the gastrointestinal tract allow for efficient nutrient uptake from restricted food sources (1, 2). By contrast, generalists require dynamic adaptation to the diverse foods that are consumed throughout life. Several features of the small intestine facilitate this flexibility. The mammalian small intestine contains the most lymphocytes of any organ and most neurons outside the brain (3, 4). In addition, the intestinal epithelium turns over every 4–5 days and contains various sensory cell types that together make up the gastrointestinal chemosensory system (5, 6). The vast majority of epithelial cells are absorptive enterocytes, which express brush border enzymes and specialized nutrient transporters involved in the uptake of luminal nutrients (7, 8). Equally important in the digestion of dietary nutrients are enzymes secreted from the pancreas into the duodenal lumen. Pancreatic amylases, lipases, and proteases initiate enzymatic digestion of carbohydrates, lipids, and proteins, respectively, following chemical and mechanical digestion in the stomach (7, 8).

The elaborate sensory capacity of the small intestine and rapid turnover of epithelial cells likely confer omnivores with flexibility in the expression of nutrient handling machinery in order to maximize digestive efficiency. Indeed, the loss of lactase expression in adult humans, which gives rise to the phenomenon of lactose intolerance, indicates that this machinery is regulated by substrate availability (9). Although individual components of digestive machinery have been demonstrated to be regulated by nutrient availability, whether entire programs can be regulated in this manner, and the mechanisms by which these programs are regulated have not been elucidated (10–13).

Results

Enteric carbohydrate transcriptional program is induced on demand

Here we tested whether and how nutrient handling machinery can be dynamically regulated by nutrient availability. Mice were fed isocaloric diets high in either carbohydrates or protein for 5 days, Small-intestine epithelial cells were then analyzed by RNAseq. This resulted in the up- and downregulation, respectively, of the enteric and pancreatic genes involved in digestion and absorption of dietary carbohydrates (hereafter referred to as "carbohydrate transcriptional program"), (Fig. 1, A to C). This program includes pancreatic and brush border enzymes, as well as monosaccharide transporters expressed in absorptive enterocytes (Fig. 1B). Expression of proteases and amino acid transporters was less sensitive to nutrient availability (Fig. 1A), presumably because unlike glucose, which can be generated endogenously through gluconeogenesis and glycogenolysis, essential amino acids can only be obtained from the diet.

We next asked whether the regulation of the carbohydrate transcriptional program was due specifically to the availability of carbohydrates, rather than differences in availability of proteins. When mice were fed diets matched for protein that differed in the ratio of fat to carbohydrates, we found increased expression of this program in mice fed a high-carbohydrate diet, independent of protein abundance (Fig. 1D). Animals fed a high-carbohydrate diet and treated with acarbose—an alpha glucosidase inhibitor that would limit carbohydrate availability for absorption—showed diminished expression of this program (Fig. 1E). Thus, carbohydrate availability drives the expression of the carbohydrate transcriptional program. The on-demand induction of this program was also preserved in germ-free mice, indicating that it does not require microbial colonization (fig. S1). Finally, mice fed a high-carbohydrate diet for 5 days showed more rapid glucose uptake after gavage and increased respiratory quotient compared with mice fed a high protein diet, indicating that the observed transcriptional changes reflect functional changes in nutrient handling (Fig. 1F to H).

Two non-mutually exclusive mechanisms could explain the transcriptional changes we observed in response to diet. These changes could arise from direct induction of this transcriptional program in differentiated enterocytes or could involve differentiation of specialized enterocytes that express this program. Though specialized enterocyte subsets have not been previously described, recent reports investigating the intestinal response to infection suggest that epithelial remodeling can underlie transcriptional responses to environmental change in this tissue (14–18). The induction kinetics of the carbohydrate transcription program were suggestive of epithelial remodeling. In "pulse-chase" experiments, where mice were fed a high-carbohydrate diet and switched to a high-protein diet for 1 or 5 days, 5-day exposure to the high protein diet was required for reduction of the carbohydrate transcriptional program (Fig. 2A). Given the 4–5-day timescale of small-intestine epithelial turnover, we hypothesized that these kinetics may reflect remodeling of the epithelial compartment in response to nutrient availability. Single-cell RNA sequencing of small-intestine epithelial cells from mice fed a high-carbohydrate or high-protein diet indicated that a number of epithelial subsets were altered in frequency following 5-day exposure to either of these diets. Thus, nutrient availability can likely alter the composition of the small-intestine epithelial compartment (Fig. 2B to C & fig. S2). Specifically, high-carbohydrate diet resulted in a reduction in the frequency of Fabp6$^+$ enterocytes and increase in the frequency of stem cells (Fig. 2C). Expression of the carbohydrate transcriptional program was enriched in Fabp1$^+$ enterocytes, suggesting that a change in the ratio of Fabp1$^+$ to Fabp6$^+$ enterocytes accounts, at least in part, for the transcriptional changes we observed (Fig. 2D). Enrichment of this program in transit amplifying cells further suggests that specialized epithelial differentiation underlies its induction. Single-molecule fluorescence in situ hybridization (FISH) experiments revealed intercellular heterogeneity in the expression of the carbohydrate transcriptional program, particularly along the crypt–villus axis (Fig. 2E). Indeed, one of the components of the carbohydrate transcriptional program, *Slc2a2*, was previously identified as a "landmark" gene for defining spatial heterogeneity in intestinal villi (19). This indicated that intercellular heterogeneity in enterocyte nutrient handling machinery reflects regional patterns in epithelial gene expression along the crypt-villus axis. The phenomenon of small-

intestine epithelial remodeling has been observed in the context of other environmental stimuli, specifically bacterial, protozoan, or helminth infection. These promote goblet cell hyperplasia, suggesting epithelial remodeling may be a general strategy by which the intestine adapts to environmental change (14–18, 20).

γδ T cells regulate the carbohydrate transcriptional program

We next investigated whether direct sensing of glucose by epithelial cells was sufficient to drive induction of the carbohydrate transcriptional program. Small intestine organoids cultured in differing concentrations of glucose did not exhibit robust induction of this program (Fig. 3A). This suggested that direct epithelial sensing was not sufficient to drive activation of this program. TRPM5-mediated taste receptor signaling and the glucose transporter SGLT1 were dispensable for induction of this program in vivo (fig. S3). Thus, we considered whether other cell types present in the intestine might contribute to its activation.

The murine small intestine contains the greatest number of lymphocytes of any tissue and several recent studies have demonstrated that resident lymphocytes can control epithelial cell fate in response to sensing of enteric infection (4, 14, 16, 17). We hypothesized that epithelial-lymphocyte circuitry may also control enteric adaptation to diet. Animals treated with an anti-Thy1 antibody to deplete T cells and innate lymphoid cells (ILCs) exhibited the impaired induction of the carbohydrate transcriptional program, suggesting the involvement of T cells or ILCs (fig. S4A). The induction of carbohydrate transcriptional program was also deficient in *Rag2*-mice a fed high-carbohydrate diet (Fig. 3B). Together, the results in *Rag2*-mice (which lack B and T cells), and in anti-Thy1 depleted mice (which lack ILCs and T cells) indicate the involvement of T cells in transcriptional response in epithelial cells. Like other barrier tissues, the small intestine contains a large number of both αβ and γδ T cells. Although the role of intestinal αβ T cells in antimicrobial and allergic defense is well established, whether they or γδ T cells play a role in the response to nutrient sensing is unexplored. When we depleted αβ T cells using an anti-TCRβ antibody, or TCRb-mice, we found that αβ T cells were dispensable for the induction of this program (Fig. 3C and fig. S4B). By contrast, mice treated with an anti-TCRγδ antibody or genetically deficient in γδ T cells exhibited defective induction of the carbohydrate transcriptional program (Fig 3D–E). Thus, γδ T cells are required for the induction of nutrient handling machinery in response to a high-carbohydrate diet.

Intestinal γδ T cells are present in two anatomically and developmentally distinct tissue compartments: the intraepithelial (IEL) and lamina propria (LPL) lymphocyte fractions (21). IELs are highly abundant, dynamic, and interact intimately with epithelial cells (4, 20). By contrast, the LP γδ T cells represent a minor fraction of the $CD45^+$ cells in this compartment. Given their proximity to epithelial cells, we hypothesized that IEL γδ T cells would be most responsive to diet. However, when we quantified the number of IELs versus LPLs by microscopy and flow cytometry, we found that LP, not IEL γδ T cells, increase in frequency and numbers during high-protein feeding (Fig. 3H and I and fig. S5). To further investigate the effect of diet on IEL versus LP γδ T cells, we performed intravital imaging studies in *Tcrd*-GFP mice. LP γδ T cell numbers increased in mice fed a high-protein diet (Fig. 3H and I and fig. S5) and IEL γδ T cells exhibited more rapid movement in mice

fed a high carb diet, suggesting that both γδ T cell compartments are affected by nutrient availability (Movie S1). Finally, we investigated whether diet might alter the proximity of γδ T cells to the intestinal crypt. We hypothesized that during a high-carbohydrate diet, γδ T cells interact with intestinal epithelial progenitors near the crypt base in order to drive the transcriptional responses and epithelial remodeling that we observed. Using 3D tissue imaging, we quantified the relative abundance of γδ T cells along the crypt–villus axis, and found an increased frequency of γδ T cells localized close to the crypt base in animals fed a high-carbohydrate diet (Fig S6). Thus, γδ T cells may influence the transcriptome and/or differentiation program of intestinal epithelial cells by interacting with epithelial progenitors in the crypt base.

We then performed RNA sequencing on αβ and γδ T cells isolated from IE and LP compartments. Unlike αβ T cells, γδ T cells from both compartments exhibited significant transcriptional responses to nutrient sensing (Fig. 3F and G). In particular, the LP γδ T cell compartment showed greatest number of differentially expressed genes in response to high carb versus high protein diet (Fig 3G and table S3 & S4), Thus, this compartment may be the most sensitive to changes in nutrient availability.

Finally, to determine whether intra- or intercompartmental heterogeneity may play a role in the transcriptional changes we observed, we performed single-cell RNA sequencing on sorted IEL and LP γδ T cells (fig. S7). We identified four transcriptionally distinct clusters of small intestine γδ T cells, reflecting IE and LP compartments (fig. S7A). Although we did not see differences in clustering in response to diet, we observed that one of the clusters we identified was enriched for genes found to be differentially regulated by diet in our bulk sequencing dataset. Thus, this cluster may be more sensitive to nutrient availability than other enteric γδ T cells (fig. S7B and C).

We then asked what upstream mediators may signal to γδ T cells during a high-carbohydrate diet. Our sequencing data did not reveal any significant changes in cytokine expression in γδ T cells (fig. S8A). However, contact-dependent signals, including components of Notch signaling, were upregulated in LP γδ T cells during a high-carbohydrate diet (fig. S8C). Intriguingly, we found that *Jagged2*, a Notch ligand, was upregulated in epithelial cells in response to high-carbohydrate diet, suggesting that Notch signaling may mediate communication between γδ T-cells and epithelial cells in response to nutrient sensing (fig. S8D). This notion was further supported by our imaging studies demonstrating that γδ T cells localize to the crypt base, where Notch ligands are more highly expressed (22), during high-carbohydrate feeding (fig. S6). To test whether Jagged2/ Notch signaling is involved in the induction of the carbohydrate transcriptional program, mice were fed a high carbohydrate diet and treated with a Jagged2 blocking antibody or isotype control. Anti-Jagged2–treated animals showed diminished expression of the carbohydrate transcriptional program as compared to isotype control treated animals. This suggested that the upregulation of *Jagged2* on epithelial cells during a high-carbohydrate diet was involved in the downstream induction of the carbohydrate transcriptional program (fig. S9A). However, anti-Jagged2 treatment did not influence the frequency or number of γδ T cells in the IEL or LP compartments (fig. S9B to D), suggesting that Notch signaling may influence γδ T cell function, but not survival.

Our sequencing data also revealed that LP γδ T cells upregulated *IL2Rb*, the coreceptor for IL-2 and IL-15, during high-carbohydrate feeding. This raised the possibility that IL-15 may regulate the γδ T-cell response to nutrient sensing (fig. S10A). Animals treated with an IL-15 blocking antibody showed diminished expression of the carbohydrate transcriptional program as compared to isotype-control–treated animals, suggesting that IL-15 signaling is an important mediator in this circuit (fig. S10B). Epithelial cell IL-15 expression was not induced by high carbohydrate diet, and anti-IL-15–treated animals showed no difference in the frequency of IEL or LP γδ T cells. Thus, IL-15 appears to be a tonic signal that maintains γδ T-cell function, rather than a nutrient-sensitive signal (fig. S10C and D).

γδ T cells regulate carbohydrate transcriptional program through control of interleukin 22

Because we did not find any differentially expressed cytokines in γδ T cells in response to diet, we assessed whether cytokines might be differentially expressed in other cell types. We found that IL-22—a cytokine known to play important roles in regulating metabolism and small intestine epithelial cell proliferation (23–26)—was upregulated in response to high protein diet. IL-22 expression was further increased in mice lacking γδ T cells (Fig. 4A). IL-22 was upregulated at the protein level ILC3s, but not Th17 cells, showed elevated IL-22 production in response to a high-protein diet and in mice lacking γδ T cells (Fig. 4B to C and fig. S11). The increased expression of IL-22 under conditions where we observed diminished expression of carbohydrate handling machinery suggested that IL-22 may be a negative regulator of this program. This was confirmed in experiments in which small intestine organoids were cultured in different concentrations of IL-22. Although small intestine organoids do not entirely recapitulate the full complement of enterocyte subsets that we observe in vivo, organoids treated with IL-22 showed alterations in the frequency of enterocytes and stem cells similar to the changes we observed in epithelial cells isolated from mice fed different diets (Fig. 4D and E and Fig. 2C). Organoids treated with IL-22 also showed dose-dependent downregulation of the carbohydrate transcriptional program, confirming that this program is negatively regulated by IL-22 (Fig. 4F). Finally, mice fed a high-protein diet and treated with anti-IL22 antibody showed expression of the carbohydrate transcriptional program at levels similar to that of mice fed a high-carbohydrate diet (Fig. 4G). Furthermore, treatment with an anti-TCRγδ antibody was unable to suppress the carbohydrate transcriptional program in *Il2*2-deficient animals (Fig. 4H). Thus, γδ T cells regulate the diet-dependent expression of carbohydrate handling machinery by suppressing expression of IL-22.

As tuft cells have recently been described to play a critical role in regulating the intestinal response to pathogens, we investigated their role in regulating the intestinal response to nutrient sensing (14, 16, 17). We found that *Pou2f3-* animals, which lack tuft cells, had decreased expression of the carbohydrate transcriptional program, which suggested that tuft cells may be an upstream regulator in this circuit (fig. S12A and B). IL-25, produced by tuft cells, is known to be a negative regulator of IL-22 expression (27). However, we did not see a significant increase in *Il25* expression in intestinal epithelial cells during high carbohydrate diet (fig. S12C). We therefore investigated the role of other soluble mediators known to be produced by tuft cells in regulating this circuit. Tuft cells express COX1/2, and are thought to produce prostaglandins (28). Because we observed that LP γδ T cells

upregulate prostaglandin receptor during high carbohydrate feeding (fig. S12D), we treated high-carbohydrate–fed animals with a COX inhibitor, indomethacin. These animals showed marked downregulation of the carbohydrate transcriptional program (fig. S12E), as well as a trend towards reduced IL-22 (Fig S12F). Thus, tuft cells may be involved in the regulation of the carbohydrate transcriptional program and may control its expression through the production of prostaglandins.

Discussion

Our studies have defined a role for γδ T cells in the regulation of epithelial transcriptional response to diet and showed that diet can alter the frequency of epithelial cell subsets. We found that machinery required for carbohydrate digestion, in both the small intestine and pancreas, can be regulated on demand in response to nutrient availability. IL-22, produced by ILC3s, plays a critical role in the regulation of specialized epithelial differentiation and expression of digestive machinery and γδ T cells can regulate its production. How γδ T cells regulate the production of IL-22 by ILC3s is an important area for future study. A recent study reported that γδ T cell–deficient animals have an increased number of another innate like lymphocyte, mucosal-associated invariant T (MAIT) cells, in the small intestine (29). This study, as well as our finding that γδ T cells limit intestinal ILC3s, suggest that γδ T cells may restrict other resident innate-like lymphocytes in the intestine. The precise molecular mechanisms that dictate the interrelationships between intestinal innate like lymphocytes, including MAIT cells, iNKT cells, ILCs, and γδ T cells represent a broad and significant area for future investigation in mucosal immunity.

This work demonstrates an important role for intestinal γδ T cells outside of antimicrobial defense, and add to emerging evidence of the tissue homeostatic role of γδ T cells (30–33). Previous studies have pointed to a role for γδ T cells in the pathogenesis of metabolic diseases, indicating that they influence the regulation of blood glucose (34–36). Our finding provides new context to these reports, suggesting that γδ T-cells may contribute to these pathologies through direct regulation of glucose uptake in the intestine The relative contributions of antigen recognition by the γδ TCR and recognition of other signals such as butyrophilins to the tissue homeostatic function of γδ T cells is an important area for future study that could be aided by identification of γδ TCR antigens that have largely remained elusive (37–39).

Our finding that IL-22 can regulate carbohydrate handling machinery accords with recent reports of its role in the regulation of lipid uptake machinery in the small intestine (40–42). Together, these findings could help to link the demonstrated role of IL-22 in organismal metabolism to its function in intestinal epithelial homeostasis and raise the possibility that IL-22 may mediate its effects on metabolism in part through its action on intestinal epithelial cells (23–26, 40, 41). This has important implications for understanding the link between intestinal function and metabolic homeostasis, as well as current efforts to apply IL-22 as a therapeutic for intestinal injury and metabolic disease. Additionally, IL-22 induction by continuous exposure to enteropathogens may contribute to diseases of nutrient malabsorption as occurs in environmental enteropathy (43).

Together with recent studies of intestinal response to helminth, bacterial, and protozoan infections (14–18, 20), our work suggests that epithelial cell–lymphocyte circuits and epithelial remodeling may be general features of adaptability to environmental change in this tissue. Our observation that nutrient uptake can be regulated by lymphocyte control of cytokine production links the regulation of nutrient uptake to the regulation of barrier defense. The finding that shared machinery can regulate both of these crucial functions in the small intestine may help explain how this tissue adjusts the balance between defense and nutrient uptake in the face of constant environmental change. Whether nutrient uptake can be regulated by other intestinal lymphocytes and cytokines in response to different environmental signals is an intriguing question for further investigation.

Materials and methods

Animals

All animal experiments were performed in accordance with institutional regulations after protocol review and approval by Yale University's Institutional Animal Care and Use Committee. The following strains were obtained from Jackson Laboratories: C57BL/6J (stock no. 000664), *Tcrd-* (stock no. 002120), *Tcrb-* (stock no. 002118), *Il22-* (stock no. 027524). *Rag2-*mice were provided by D, Schatz (Yale University), *Tcrd-*GFP mice were provided by D. Mucida (Rockefeller University). *Trpm5-*mice were provided by W. Garrett (Harvard University). *Pou2f3-*mice were provided by C. Wilen (Yale University). Germ-free C57BL/6 mice were bred and maintained in Class Biologically Clean isolators. Dietary interventions and other experimental procedures were performed in microisolator cages (Isocage P; Techniplast). Females aged 7–12 weeks were used for all experiments and were euthanized by cervical dislocation at ZT8.

For antibody treatment experiments, animals were injected intravenously with 500 μg of anti-Thy1 (clone 30H12; BioXCell #BP0066) or anti-keyhole lymphocyanin isotype control (clone LTF-2; BioXCell #BP0090); or 200 μg anti-TCRβ (clone H57-597; BioXCell #BE0102), anti-TCRγδ (clone UC7-1365: BioXCell #BE0070), or Armenian hamster isotype control (BioXCell #BE0091) on days −1, 0, 2, and 4 of each experiment. One hundred μg anti-IL-22 (clone IL22JOP; ThermoFisher #16-7222-82) or Rat IgG2a isotype control (clone eBR2a; ThermoFisher #16-4321-82) was injected intraperitoneally on days 0, 2, and 4 of each experiment.

SGLT1 inhibitor phloridzin (SigmaAldrich) was administered via subcutaneously every 12 hours for the duration of each experiment. Animals received 5 mg phloridzin or vehicle (10% EtOH, 15% DMSO, 75% PBS) per injection. Acarbose (Cayman Chemical Co) was administered by daily gavage for the duration of the experiment. Animals received 25 μg acarbose or PBS per treatment. To quantify glucose uptake, Animals were fasted for 4 hours and then administered 30 mg D-glucose by gavage. Blood glucose was measured every 5 min following injection using a OneTouch handheld glucometer. For metabolic cage experiments, animals were individually housed in Promethion High-Definition Multiplexed Respirometry Cages (Sable Systems International). After 3 days of acclimatization, special diets were introduced, and animals were monitored for VO_2 and VCO_2 for 5 days. Purified,

specialized animal diets were purchased from Envigo. Diet ingredients and nutritional information is summarized in Table S5. Diets were sterilized by irradiation.

Epithelial cell and lamina propria isolation (for qPCR and flow cytometry)

Single-cell suspensions of small intestine epithelium and lamina propria were prepared as described (44). Briefly, small intestine was isolated, opened longitudinally, and contents rinsed in PBS following removal of Peyer's Patches. Tissue was then cut into 2–3-mm segments and incubated in RPMI media (ThermoFisher) containing 5 mM EDTA, DTT, and 3% FBS at 37°C with 5% CO_2 for 20 min with agitation. Pieces of intestine were then washed in RPMI containing 2 mM EDTA to separate the epithelial fraction. Epithelial cell RNA was isolated from this fraction. In cases where intraepithelial lymphocytes (IELs) were stained, the epithelial fraction was subjected to 30% Percoll density gradient by centrifugation (Sigma Aldrich). Lamina propria digestion was performed using Liberase (Roche) and DNAse (Sigma Aldrich) in RPMI for 30 min at 37°C with 5% CO_2. Digested tissue was sequentially strained through 70 uM and 40 uM strainers, washed in RPMI containing 3% FBS, and cells stained for further analysis. Epithelial cells used for scRNAseq were isolated as described (18). Small intestines were isolated, opened longitudinally, and rinsed in cold PBS. 2 millimeter tissue fragments were incubated in 20 mM EDTA in PBS for 2–3 hours. The single-cell suspension was then passed through a 40 μm filter and stained for isolation by fluorescence-activated cell sorting (FACS) (Astrios) for droplet-based scRNA-seq (below).

Flow cytometry

Single-cell suspensions were treated with anti-CD16/32 (Fcblock) (ThermoFisher #14-9161-73) and stained with ZombieYellow Fixable Live/Dead dye (Biolegend) and the following antibodies: PE-Cy7-anti-CD326/EpCAM (clone 9C4; Biolegend # 118216), BUV395-anti-CD45 (clone 30-F11; BD Biosciences # 564279), PE-anti-TCRγδ (clone GL3; ThermoFisher #12-5711-82), APC-anti-TCRβ (clone H57-597; Biolegend #109212), PE-Cy7-anti-TCRβ (clone H57-597; Biolegend # 109221), FITC-anti-CD90.2 (clone 30-H12; BD Biosciences 3133962), APC-anti-CD90.2 (clone 5302.1; ThermoFisher 17-0902-81), BV605-anti-CD4 (clone RM4-5; Biolegend # 100547), 7AAD (ThermoFisher), anti-PE-anti-CD31 (clone 390; ThermoFisher # 12-0311-82), AlexaFluor 647-anti-IL-22 (clone IL22JOP; ThermoFisher #17-7222-80), PE-anti-RORgt (clone B2D; ThermoFisher # E14326-107). "Lineage" staining was performed using PE-Cy7-Streptavidin (ThermoFisher #25-4317-82) or BV421-Streptavidin (BD Biosciences #563259) and the following biotinylated antibodies: anti-CD3 (clone 145-2C11; ThermoFisher # 13-0031-85), anti-CD5 (clone 53-7.3; BD Biosciences # 553018), anti-CD8a (clone 53-6.7; ThermoFisher # 13-0081-82), anti-CD19 (clone 1D3; BD Biosciences #553784), anti-CD11b (clone M1/70; ThermoFisher #13-0112-85), anti-CD11c (clone N418; ThermoFisher # 13-0114-82), anti-CD45R (clone RA3-6B; Biolegend # 103204), anti-CD49b (clone DX5; BD Biosciences # 553856), anti-F4/80 (clone BM8; ThermoFisher # 13-4801-85), anti-FcER1 (clone MAR-1; ThermoFisher 13-5898-85), anti-Gr1 (clone RB6-8C5; BD Biosciences # 13-5931-85), anti-Nk1.1 (clone PK136; ThermoFisher # 13-5941-82), anti-Ter119 (clone TER-119; ThermoFisher # 13-5921-81). Stimulation and intracellular cytokine staining was performed as in (44). Cells were stimulated for 2 hours

at 37°C with 50 ng/ml phorbol 12-myristate 13-acetate (Sigma Aldrich), 1 μM ionomycin (Cell Signaling Technologies) in the presence of GolgiPlug (BD Biosciences). Staining for intracellular cytokines and transcription factors was performed using FoxP3/Transcription Factor Staining Buffer Set (ThermoFisher). Flow cytometry was performed using a BD LSRII analyzer. Data were analyzed using FlowJoX (BD Biosciences). Gates were drawn according to fluorescence minus one (FMO) controls.

Cell sorting

For bulk T cell RNAseq—Stained cells were sorted using a BD FACSAriaII. Cells were gated on live, $CD45^+$, $EpCAM^-$, single-cells, and sorted into $TCRb^+TCRgd^-$ and $TCRb^-TCRgd^+$ populations. Cells were collected in RLT lysis buffer (Qiagen) containing 1% beta-mercaptoethanol.

For plate-based scRNAseq—Cells were sorted using parameters described above. Single γδ T cells were sorted into individual wells of a 96-well plate containing TCL lysis buffer (Qiagen) with 1% beta-mercaptoethanol. Immediately after sorting, plates were spun down and frozen at −80°C until library preparation.

For droplet based scRNAseq—FACS (Astrios) was used to sort cells into Eppendorf tubes containing PBS with 0.1% BSA and stored on ice until library preparation. Cells were gated on live, $CD31^-$, $Ter119^-$, $CD45^-$, $EpCAM^+$ single cells.

qPCR analysis

Total RNA was purified from epithelial cells using DiretZol RNA Miniprep Plus Kit (Zymo). Total RNA was purified from organoids using RNEasy Plus Micro Kit (Qiagen). Total RNA was quantified by NanoDrop (ThermoFisher) and added to reverse transcriptase reaction using SMART MMLV Reverse Transcriptase (Takara Bio) according to the manufacturer's instructions. qPCR was performed with PerfeCTa SYBR Green (Quanta Bio) using BioRad CFX96 platform. Expression was calculated relative to Rpl13a. A list of primers is provided in table S6.

Intestinal organoid cultures

Crypts were isolated from whole small intestine as follows. The small intestine was extracted and rinsed in cold PBS. The tissue was opened longitudinally and sliced into small fragments roughly 0.2-cm long. The tissue was incubated in 20 mM EDTA-PBS on ice for 90 min, while shaking every 30 min. The tissue was then shaken vigorously and the supernatant was collected as a fraction in a new conical tube. Next, the tissue was incubated in fresh EDTA-PBS and a new fraction was collected every 30 min. Fractions were collected until the supernatant consisted almost entirely of crypts. The final fraction (enriched for crypts) was filtered through a 70-μm filter, washed twice in PBS, centrifuged at 300g for 3 min, and dissociated with TrypLE Express (Invitrogen) for 1 min at 37°C. Following crypt isolation from the whole small intestine of both male and female mice, the single-cell suspension was resuspended in Matrigel (BD Bioscience) with 1 μM Jagged-1 peptide (Ana-Spec). Roughly 300 crypts embedded in 25 μl of Matrigel were seeded onto each well of a 24-well plate. Once solidified, the Matrigel was incubated in 600 μl culture

medium (Advanced DMEM/F12, Invitrogen) with streptomycin–penicillin and glutamatax and supplemented with EGF (100 ng/ml, Peprotech), R-Spondin-1 (600 ng/mL, R&D), Noggin (100 ng/mL, Prepotech), Y-276432 dihydrochloride monohydrate (10 μM, Tochris), N-acetyl-1-cysteine (1 μM, Sigma-Aldrich), N2 (1X, Life Technologies), B27 (1X, Life Technologies) and Wnt3A (25 ng/mL, R&D Systems). Fresh media was replaced on day 3, and organoids were passaged by dissociation with TrypLE and re-suspended in new Matrigel on day 6 with a 1:3 split ratio.

Intravital imaging

Terminal ileum of live *Tcrgd*-GFP mice were imaged as described previously (20). Animals were anesthetized using isoflurane before surgery and injected intravenously with Hoechst dye. Ten minutes after induction of anesthesia, animals were placed on a platform heated to 37°C. A small incision was made in the abdomen and a loop of terminal ileum was exposed, opened longitudinally, and contents removed. The platform was then transferred to a FV1000MPE Twin upright multiphoton (Olympus) heated stage, and images collected with time lapse of ± 30 s with a total acquisition time of 20 min.

Whole mount tissue imaging

Imaging of terminal ileum and duodenum was performed as previously described (20). Tissues were isolated from TCRγδ-GFP after intravenous injection of Hoechst dye. Contents were removed, and tissue was fixed in 4% PFA overnight at 4°C. Tissues were washed in PBS and placed in FocusClear (Celeplorer Labs Co) solution for 30 min at room temperature. Samples were then mounted on 3D printed slides and imaged using a FV1000MPE Twin upright multiphoton microscope (Olympus).

T cell imaging analysis

T cells located in the lamina propria (dense nucleated area below epithelial basement membrane) where manually counted with Fiji Cell Counter, area scanned from each tissue was 509 × 509 μm over 41 *z*-stacks of 5-μm step size, starting in the tip of the villus down to the crypts. Total T cell count was performed with Fiji TrackMate v5.1(45) based on a cell size of 10 μm and GFP signal threshold of 1500 units over all *z*-planes. Total nucleated cells were counted with Fiji TrackMate v5.1 with cell size of 10 μm and DAPI signal threshold of 500 units over all *z*-planes.

RNA fluorescence in situ hybridization (FISH)

An RNAscope® Multiplex Fluorescent V2 (ACD, 323100) detection kit was used according to the manufacturer's instructions. Paraffin-embedded sections were boiled in the target retrieval solution at ~100°C for 15 min and incubated in Protease Plus solution at 40°C for 15 min. Probes for the following genes in Mus musculus were used: Mm-Sis (573021), Mm-Slc2a2-E11-C2 (439891-C2), and Mm-Slc5a1-C3 (468881-C3), and slides were stained with DAPI. Images and *z*-stacks were acquired with a 20x objective using a Zeiss LSM900 confocal microscope and Zen software (Zeiss). When indicated, maximum intensity projections were generated using Zen. Images and *z*-stacks were acquired with a

20x objective using a Zeiss LSM900 confocal microscope equipped with an Airyscanner2 and Zen software (Zeiss).

Statistics

With the exception of sequencing analysis, all statistical analyses were performed in GraphPad Prism7. Statistical information is included in figure legends.

Plate-based single-cell RNAseq & analysis

Plate-based single cell RNAseq was performed as previously described (15). RNA-seq libraries were constructed following SMART-seq2 protocol (46). RNA clean-up was performed using RNACleanXP beads (Agencourt). Reverse transcription was performed using Maxima H-Reverse Transcriptase (ThermoFisher) followed by whole transcription amplification (WTA) using KAPA HiFi HotStart PCR ReadyMix (KAPA Biosystems). Cleanup of WTA products was performed using AMPure XP beads (Agencourt). DNA quantification was performed using a High Sensitivity DNA Qubit kit and Qubit analyzer (Life Technologies). Fragment sizes were assessed with a high-sensitivity DNA chip (Agilent). Indexing and library preparation was performed using the Nextera XT DNA Library Prep Kit (Illumina). The libraries were sequenced on Illumina NextSeq 500 (38×38 bp paired-end run). A total of 1536 cells were sequenced.

Nextseq 500 base call files were demultiplexed into FASTQ files using bcl2fast2 (Illumina). FASTQ files were used to quantify transcripts for each single cell using kallisto (47) Transcript TPMs for each gene were summed to obtain gene level TPMs. A matrix containing the TPMs for each gene for each cell was used as input for the single-cell RNA-seq analysis software package Seurat (48). Genes were excluded from the analysis if they had the prefix "GM" or were expressed in fewer than 10 cells. Cells were included in the analysis if they had non-zero TPMs for the Tcell associated genes *Ptprc, Cd3d,* and *Cd3e* and expressed at least 1000 genes. After quality control, a total of 361 cells were included in the analysis. Seurat was used to classify cells into clusters and to determine what marker genes defined the clusters. The Seurat FindClusters function was run using a resolution parameter of 0.6. T-SNE and Violin Plots were created using Seurat.

Bulk RNAseq & Analysis

RNA was isolated from sorted T cells using RNEasy Plus Micro Kit (Qiagen), and library preparation performed using SMART-seq2 protocol as described above. RNA was isolated from epithelial cells using DirectZol RNA Miniprep Plus Kit with on-column DNAse digestion according to the manufacturer's instructions (Zymo). Sequencing libraries were constructed using Illumina TruSeq Library Prep Kit and sequenced on Illumina NextSeq 500 (38×38 bp paired-end run).

Sequencing reads were aligned to the mm10 mouse transcriptome (GRCm38 ensembl; cDNA and ncRNA) and quantified by Kallisto (v0.45.0) with a k-mer index 25 and 60 bootstrapping (47). The expression of transcript was calculated in TPM (transcripts per million). When multiple transcripts match to the same gene, the expression of the gene is calculated by summing the TPM of all matched transcripts. TPM's of 3–4 biological

replicates were averaged for each sample. Statistical analyses for differentially expressed genes were performed by Sleuth(49).

Droplet-based scRNA-Seq & Analysis

Single-cell suspensions were loaded onto 3′ library chips as per the manufacturer's protocol for the Chromium Single Cell 3′ Library (V3) (10X Genomics; PN-120233). Briefly, single cells were partitioned into Gel Beads in Emulsion (GEMs) in the Chromium instrument with cell lysis and barcoded reverse transcription of RNA, followed by amplification, enzymatic fragmentation and 5′ adaptor and sample index attachment. Each 10X channel contained either one mouse or a pool of three mice for each condition to account for variations between samples and were loaded on Chromium Single Cell Platform. In addition, both the epithelial fraction and the lamina propria fraction were loaded to the same 10X channel with 7:1 ratio, receptively. An input of 10,000 single cells per sample was added to each channel with a recovery rate of approximately 5000 cells per sample. Libraries were sequenced on an Illumina Nextseq.

Processing FASTQ reads into gene expression matrices

Cell Ranger v2.0 and Cumulus v0.7.0 (50) were used to demultiplex the FASTQ reads, align them to the mm10 mouse transcriptome, and to generate the feature-count matrix for the cell-hashing data, using the "cumulus_hashing_cite_seq" workflow described in the Cumulus documentation.

The output of this pipeline is a digital gene expression (DGE) matrix for each sample, which records the number of UMIs for each gene that are associated with each cell barcode. As described previously (51), DGE matrices were filtered to remove low quality cells, defined as cells in which fewer than 500 different genes were detected. A total of 122,492 cells were used for downstream analysis. To account for differences in sequencing depth across cells, UMI counts were normalized by the total number of UMIs per cell and converted to transcripts-per-10,000 (henceforth "TP10K").

Cell clustering overview—To cluster single cells into distinct cell subsets, we followed a previously outlined general procedure (15) with additional modifications. This workflow includes the following steps: partitioning cells into epithelial, stromal, and immune compartments, followed by clustering the cells within each compartment, which entails the selection of "variable" genes, batch correction, dimensionality reduction (PCA), and graph clustering. Each step of this workflow is detailed below.

Partitioning cells into epithelial, stromal, and immune compartments—Cells were partitioned into epithelial, stromal, and immune compartments based on the expression of known marker genes. First, we clustered the cells by their gene expression profiles (with the clustering procedure below). The clusters were scored for the following gene signatures: epithelial cells (*Epcam, Krt8, Krt18*), stromal cells (*Col1Aa1, COl1a2, COl6a1, COl6a2, Vwf, Plvap, Cdh5, S100b*), and immune cells (*Cd52, Cd2, Cd3d, Cd3g, Cd3e, Cd79a, Cd79b, Cd14, Cd16, Cd68, Cd83, Csf1r, Fcer1g*). Signature scores were calculated as the mean $\log_2$(TP10K+1) across all genes in the signature. Each cluster was assigned to the

compartment of its maximal score and all cluster assignments were manually inspected to ensure the accurate segregation of cells. Finally, the cells within each compartment were assembled into three DGE matrices, comprising all epithelial cells, all stromal cells, and all immune cells. The epithelial cells were retained for further downstream analysis.

Variable gene selection—To identify variable genes within a sample, we first calculated the mean (μ) and the coefficient of variation (CV) of expression of each gene. Genes were then grouped into 20 equal-frequency bins (ventiles) according to their mean expression levels. LOESS regression was used to fit the relationship, $\log(CV) \sim \log(\mu)$, and the 1500 genes with the highest residuals were evenly sampled across these expression bins. To extend this approach to multiple samples, we performed variable gene selection separately for each sample to prevent "batch" differences between samples from unduly impacting the variable gene set. A consensus list of 1500 variable genes was then formed by selecting the genes with the greatest recovery rates across samples, with ties broken by random sampling. This consensus gene set was then pruned through the removal of all ribosomal, mitochondrial, immunoglobulin, and HLA genes, which were found to induce unwanted batch effects in some samples in downstream clustering steps.

Batch correction—We observed substantial variability between cells that had been obtained from different mice, which likely reflects a combination of technical and biological differences. In some cases, these "batch effects" led to cells clustering first by mouse, rather than by cell type or cell state.

To eliminate these batch differences, we ran ComBat (52) with default parameters on the $\log_2(\text{TP10K+1})$ expression matrix, allowing cells to be clustered by cell type or cell state. Importantly, these batch-corrected data were only used for the PCA and all steps relying on PCA (e.g. clustering, diffusion map, t-SNE visualization); all other analyses (e.g. differential expression analysis) were based on the original expression data.

Dimensionality reduction, graph clustering, and t-SNE visualization—We ran low-rank PCA on the variable genes of the batch-corrected expression matrix, chosen as described above. We then applied Phenograph (53) to the k-NN graph defined using PCs 1 to 20 and $k = 250$, which was selected through close inspection of the data. Finally, the Barnes - Hut t-distributed stochastic neighbor embedding (t-SNE) algorithm was run on the PCs with perplexity = 20 and for 1000 iterations to produce two-dimensional embeddings of the data for visualization.

Identifying statistically significant differences in cell proportions—A major concern with the comparison of cell proportions in scRNA-Seq data is that they are not independent of each other. Because all proportions sum to 1, an increase in the proportion of one cell subset will necessarily lead to a decrease in the proportions of other cell subsets. To account for these dependencies, we used a Dirichlet-multinomial regression model, which tests for differences in cell composition between conditions (e.g., high carb diet versus high protein diet), while accounting for the proportions of all of the other cell subsets. This regression model and its associated P-values were calculated using the "DirichReg" function in the DirichletReg R package.

Supplementary Material

Refer to Web version on PubMed Central for supplementary material.

Acknowledgements:

Data and materials availability:

Sequencing data is available via NCBI GEO (GSE145857). All data is available in the main text or the supplementary materials.

References and notes

1. Karasov WH, Martinez del Rio C, Caviedes-Vidal E, Ecological physiology of diet and digestive systems. Annu Rev Physiol 73, 69–93 (2011). [PubMed: 21314432]

2. Karasov WH, Douglas AE, Comparative digestive physiology. Compr Physiol 3, 741–783 (2013). [PubMed: 23720328]

3. Furness JB, The enteric nervous system and neurogastroenterology. Nat Rev Gastroenterol Hepatol 9, 286–294 (2012). [PubMed: 22392290]

4. Hoytema van Konijnenburg DP, Mucida D, Intraepithelial lymphocytes. Curr Biol 27, R737–R739 (2017). [PubMed: 28787597]

5. Gribble FM, Reimann F, Function and mechanisms of enteroendocrine cells and gut hormones in metabolism. Nature Reviews Endocrinology 15, 226–237 (2019).

6. van der Flier LG, Clevers H, Stem cells, self-renewal, and differentiation in the intestinal epithelium. Annu Rev Physiol 71, 241–260 (2009). [PubMed: 18808327]

7. Barrett KE. (McGraw Hill Education/Medical, New York:, 2014), pp. xii, 321 pages:.

8. Boron WF, Boulpaep EL, Eds. (Saunders/Elsevier, Philadelphia, PA:, 2012), pp. xiii, 1337 pages:.

9. Misselwitz B, Butter M, Verbeke K, Fox MR, Update on lactose malabsorption and intolerance: pathogenesis, diagnosis and clinical management. Gut 68, 2080–2091 (2019). [PubMed: 31427404]

10. Mochizuki K, Honma K, Shimada M, Goda T, The regulation of jejunal induction of the maltase-glucoamylase gene by a high-starch/low-fat diet in mice. Mol Nutr Food Res 54, 1445–1451 (2010). [PubMed: 20425755]

11. Goda T, Raul F, Gosse F, Koldovsky O, Effects of a high-protein, low-carbohydrate diet on degradation of sucrase-isomaltase in rat jejunoileum. Am J Physiol 254, G907–912 (1988). [PubMed: 3287954]

12. Cezard JP, Broyart JP, Cuisinier-Gleizes P, Mathieu H, Sucrase-isomaltase regulation by dietary sucrose in the rat. Gastroenterology 84, 18–25 (1983). [PubMed: 6847846]

13. Goda T, Regulation of the expression of carbohydrate digestion/absorption-related genes. Br J Nutr 84 Suppl 2, S245–248 (2000). [PubMed: 11242478]

14. Howitt MR et al. , Tuft cells, taste-chemosensory cells, orchestrate parasite type 2 immunity in the gut. Science 351, 1329–1333 (2016). [PubMed: 26847546]

15. Haber AL et al. , A single-cell survey of the small intestinal epithelium. Nature 551, 333–339 (2017). [PubMed: 29144463]

16. von Moltke J, Ji M, Liang HE, Locksley RM, Tuft-cell-derived IL-25 regulates an intestinal ILC2-epithelial response circuit. Nature 529, 221–225 (2016). [PubMed: 26675736]

17. Schneider C et al. , A Metabolite-Triggered Tuft Cell-ILC2 Circuit Drives Small Intestinal Remodeling. Cell 174, 271–284 e214 (2018). [PubMed: 29887373]

18. Biton M et al. , T Helper Cell Cytokines Modulate Intestinal Stem Cell Renewal and Differentiation. Cell 175, 1307–1320 e1322 (2018). [PubMed: 30392957]

19. Moor AE et al. , Spatial Reconstruction of Single Enterocytes Uncovers Broad Zonation along the Intestinal Villus Axis. Cell 175, 1156–1167.e1115 (2018). [PubMed: 30270040]

20. Hoytema van Konijnenburg DP et al. , Intestinal Epithelial and Intraepithelial T Cell Crosstalk Mediates a Dynamic Response to Infection. Cell 171, 783–794 e713 (2017). [PubMed: 28942917]

21. Vantourout P, Hayday A, Six-of-the-best: unique contributions of gammadelta T cells to immunology. Nature reviews. Immunology 13, 88–100 (2013).

22. Gehart H, Clevers H, Tales from the crypt: new insights into intestinal stem cells. Nat Rev Gastroenterol Hepatol 16, 19–34 (2019). [PubMed: 30429586]

23. Zenewicz LA et al. , Innate and Adaptive Interleukin-22 Protects Mice from Inflammatory Bowel Disease. Immunity 29, 947–957 (2008). [PubMed: 19100701]

24. Wang X et al. , Interleukin-22 alleviates metabolic disorders and restores mucosal immunity in diabetes. Nature 514, 237–241 (2014). [PubMed: 25119041]

25. Lindemans CA et al. , Interleukin-22 promotes intestinal-stem-cell-mediated epithelial regeneration. Nature 528, 560–564 (2015). [PubMed: 26649819]

26. Gronke K et al. , Interleukin-22 protects intestinal stem cells against genotoxic stress. Nature 566, 249–253 (2019). [PubMed: 30700914]

27. Sawa S et al. , RORγt+ innate lymphoid cells regulate intestinal homeostasis by integrating negative signals from the symbiotic microbiota. Nature immunology 12, 320–326 (2011). [PubMed: 21336274]

28. O'Leary CE, Schneider C, Locksley RM, Tuft Cells—Systemically Dispersed Sensory Epithelia Integrating Immune and Neural Circuitry. Annual review of immunology 37, 47–72 (2019).

29. Constantinides MG et al. , MAIT cells are imprinted by the microbiota in early life and promote tissue repair. Science 366, (2019).

30. Ribeiro M et al. , Meningeal γδ T cell–derived IL-17 controls synaptic plasticity and short-term memory. Science Immunology 4, eaay5199 (2019). [PubMed: 31604844]

31. Hong MJ et al. , Protective role of gammadelta T cells in cigarette smoke and influenza infection. Mucosal immunology 11, 894–908 (2018). [PubMed: 29091081]

32. Crawford G et al. , Epithelial damage and tissue gammadelta T cells promote a unique tumor-protective IgE response. Nature immunology 19, 859–870 (2018). [PubMed: 30013146]

33. Kohlgruber AC et al. , gammadelta T cells producing interleukin-17A regulate adipose regulatory T cell homeostasis and thermogenesis. Nature immunology 19, 464–474 (2018). [PubMed: 29670241]

34. He S et al. , Gut intraepithelial T cells calibrate metabolism and accelerate cardiovascular disease. Nature 566, 115–119 (2019). [PubMed: 30700910]

35. Markle JG et al. , gammadelta T cells are essential effectors of type 1 diabetes in the nonobese diabetic mouse model. Journal of immunology 190, 5392–5401 (2013).

36. Mehta P, Nuotio-Antar AM, Smith CW, gammadelta T cells promote inflammation and insulin resistance during high fat diet-induced obesity in mice. Journal of leukocyte biology 97, 121–134 (2015). [PubMed: 25395302]

37. Willcox BE, Willcox CR, gammadelta TCR ligands: the quest to solve a 500-million-year-old mystery. Nature immunology 20, 121–128 (2019). [PubMed: 30664765]

38. Bas A et al. , Butyrophilin-like 1 encodes an enterocyte protein that selectively regulates functional interactions with T lymphocytes. Proceedings of the National Academy of Sciences of the United States of America 108, 4376–4381 (2011). [PubMed: 21368163]

39. Melandri D et al. , The gammadeltaTCR combines innate immunity with adaptive immunity by utilizing spatially distinct regions for agonist selection and antigen responsiveness. Nature immunology 19, 1352–1365 (2018). [PubMed: 30420626]

40. Mao K et al. , Innate and adaptive lymphocytes sequentially shape the gut microbiota and lipid metabolism. Nature 554, 255–259 (2018). [PubMed: 29364878]

41. Talbot J et al. , VIP-producing enteric neurons interact with innate lymphoid cells to regulate feeding-dependent intestinal epithelial barrier functions. bioRxiv, 721464 (2019).

42. Talbot J et al. , Feeding-dependent VIP neuron–ILC3 circuit regulates the intestinal barrier. Nature 579, 575–580 (2020). [PubMed: 32050257]

43. Korpe PS, Petri WA Jr., Environmental enteropathy: critical implications of a poorly understood condition. Trends Mol Med 18, 328–336 (2012). [PubMed: 22633998]

44. Spencer SP et al. , Adaptation of innate lymphoid cells to a micronutrient deficiency promotes type 2 barrier immunity. Science 343, 432–437 (2014). [PubMed: 24458645]

45. Tinevez JY et al. , TrackMate: An open and extensible platform for single-particle tracking. Methods (San Diego, Calif.) 115, 80–90 (2017). [PubMed: 27713081]

46. Picelli S et al. , Full-length RNA-seq from single cells using Smart-seq2. Nature protocols 9, 171–181 (2014). [PubMed: 24385147]

47. Bray NL, Pimentel H, Melsted P, Pachter L, Near-optimal probabilistic RNA-seq quantification. Nat. Biotechnol. 34, 525–527 (2016). [PubMed: 27043002]

48. Butler A, Hoffman P, Smibert P, Papalexi E, Satija R, Integrating single-cell transcriptomic data across different conditions, technologies, and species. Nature biotechnology 36, 411–420 (2018).

49. Pimentel H, Bray NL, Puente S, Melsted P, Pachter L, Differential analysis of RNA-seq incorporating quantification uncertainty. Nat Methods 14, 687–690 (2017). [PubMed: 28581496]

50. Gaublomme JT et al. , Nuclei multiplexing with barcoded antibodies for single-nucleus genomics. Nat Commun 10, 2907 (2019). [PubMed: 31266958]

51. Smillie CS et al. , Intra- and Inter-cellular Rewiring of the Human Colon during Ulcerative Colitis. Cell 178, 714–730.e722 (2019). [PubMed: 31348891]

52. Johnson WE, Li C, Rabinovic A, Adjusting batch effects in microarray expression data using empirical Bayes methods. Biostatistics 8, 118–127 (2007). [PubMed: 16632515]

53. Levine JH et al. , Data-Driven Phenotypic Dissection of AML Reveals Progenitor-like Cells that Correlate with Prognosis. Cell 162, 184–197 (2015). [PubMed: 26095251]

54. Huang da W, Sherman BT, Lempicki RA, Systematic and integrative analysis of large gene lists using DAVID bioinformatics resources. Nature protocols 4, 44–57 (2009). [PubMed: 19131956]
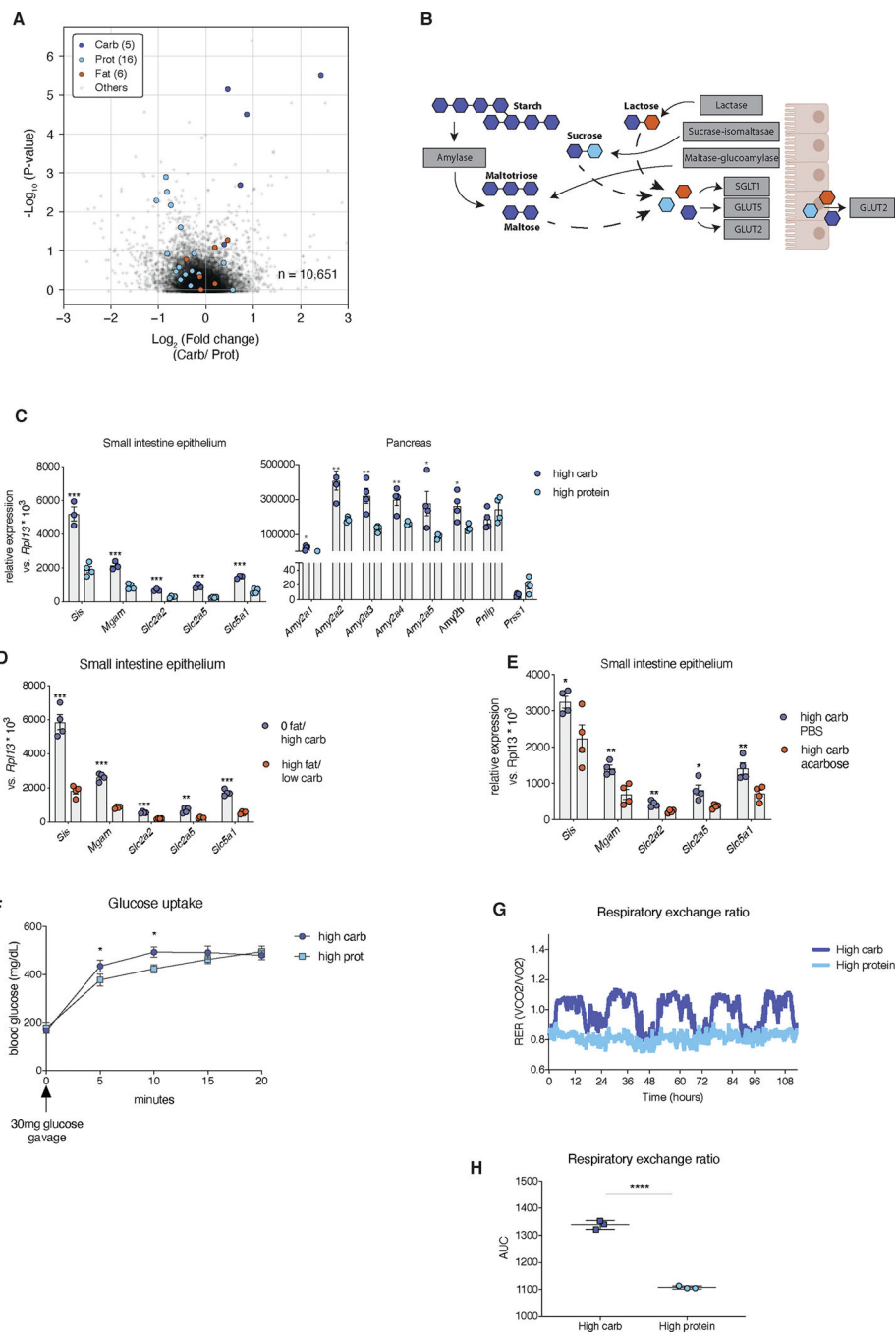
Figure 1. Carbohydrate availability drives expression of carbohydrate transcriptional program.
(**A**) Volcano plot showing differentially regulated genes in small intestine epithelial cells in response to a high-carbohydrate or high-protein diet. A full list of genes can be found in table S1. Colored circles correspond to transcripts for brush border enzymes and transporters involved in digestion of carbohydrates, protein, or lipids. (**B**) Pancreatic enzymes, brush border enzymes, and monosaccharide transporters involved in digestion and absorption of carbohydrates, encoded by carbohydrate transcriptional program. (**C to E**) qPCR analysis of carbohydrate transcriptional program expression in small-intestine epithelium and pancreas

of mice fed a high-carbohydrate or high-protein diet, **(C)** a high-carbohydrate or high-fat diet **(D),** or a high carbohydrate diet and treated with the alpha-glucosidase inhibitor acarbose **(E). (F)** glucose uptake in mice fed high carb or high protein diet. **(G)** respiratory exchange ratio and corresponding area under the curve **(H)** in mice fed high carbohydrate or high protein diet. n=3–4 mice per group. p-values in (A) calculated using Sleuth. Data represent mean ± SEM. *P*-values in B-H calculated by Student's *t* test. *$P<0.05$, **$P<0.01$, ***$P<0.001$. Data are representative of at least two independent experiments.
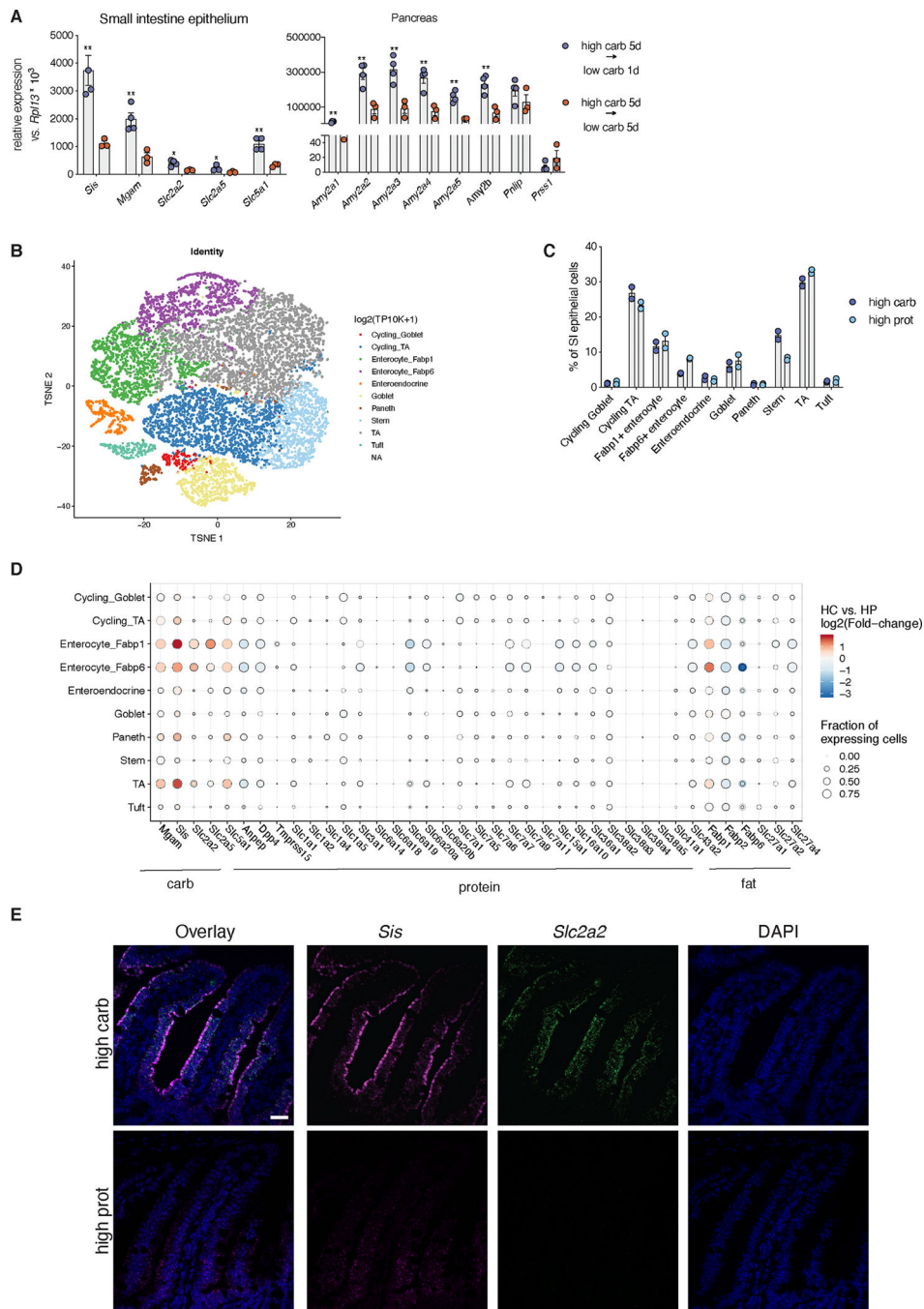
Figure 2. Diet alters composition of epithelial compartment.
(**A**) Expression of carbohydrate transcriptional program in small intestine epithelium and pancreas in mice fed high carbohydrate diet for 5 days and subsequently switched to high protein diet for 1 or 5 days (**B**) t-SNE plots of major epithelial cell subsets with 10,000 cells displayed (**C**) Frequency of epithelial cell subsets in (B) during high-carbohydrate or high-protein diets. (**D**) Differential expression of nutrient handling machinery for carbohydrates, protein, and fat. A full list of genes can be found in table S2. (**E**) Single-molecule fluorescence in situ hybridization imaging of indicated carbohydrate program transcripts

in jejunum isolated from mice fed high carbohydrate or high protein diet for 5 days. Scale bar = 100 μm. *P*-values in (A) calculated using Student's *t* test. Data represent mean ± SEM. ***P<0.001. Data in A are representative of at least two independent experiments with n=3–4 mice per group. Data in B-D are from a single experiment with four mice per group pooled into two samples.
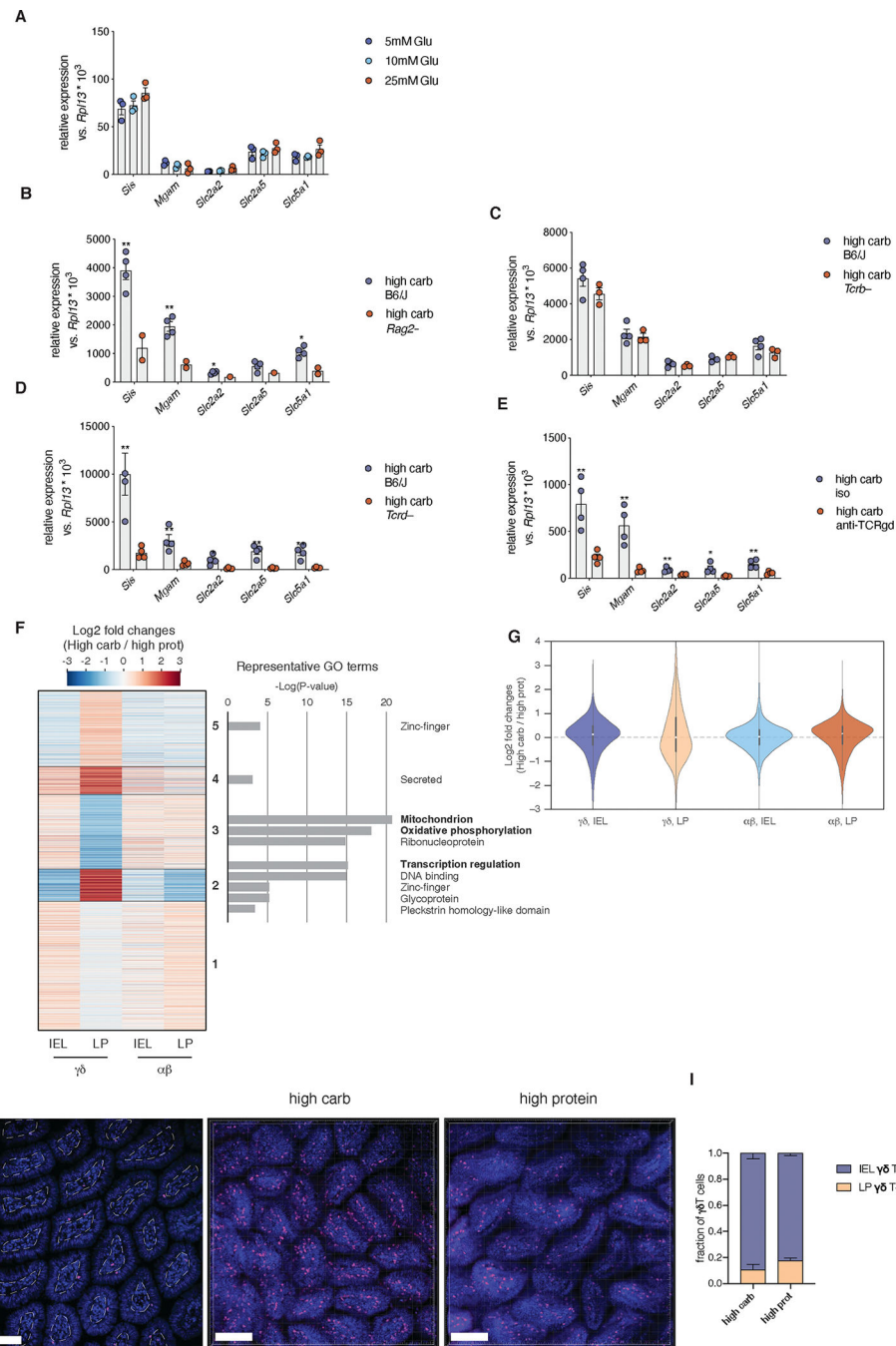
Figure 3. γδ T cells are required for induction of carbohydrate transcriptional program.
(**A**) Expression of carbohydrate transcriptional program in small intestine organoids cultured with indicated varying concentrations of glucose (**B-E**) Expression of carbohydrate transcriptional program in small intestine epithelial cells from mice fed high carbohydrate diet under indicated genotypes and treatment conditions (**F**) Heatmap showing fold changes in transcript levels in lamina propria (LP) or intraepithelial (IEL) γδ or αβ T cells isolated from small intestine of mice fed high carbohydrate or high protein diet. Genes were grouped by K-means clustering and functionally analyzed by DAVID (54). Full gene lists in table

S3. (n=3–4). **(G)** Transcriptomic reprogramming of γδ T cells in lamina propria. Violin plots showing the changes in RNA expression between high-carbohydrate and high-protein diets. The plots were scaled with the same area. The white dot represents the median. **(H)** Representative images of cleared ileum tissue from TCRγδ-GFP mice fed high carbohydrate or high protein diet. Dotted lines indicate border used to delineate IEL from LP region. γδ T cells are pseudocolored red. Scale bar = 100μm **(I)** quantification of LP and IEL γδ T-cells from cleared tissue images. n=3–4 mice per group. Data represent mean ± SEM. *P*-values in A-E calculated by Student's *t* test. *P<0.05, **P<0.01, ***P<0.001. Data are representative of at least two independent experiments (except in F-G, which represent a single sequencing experiment).
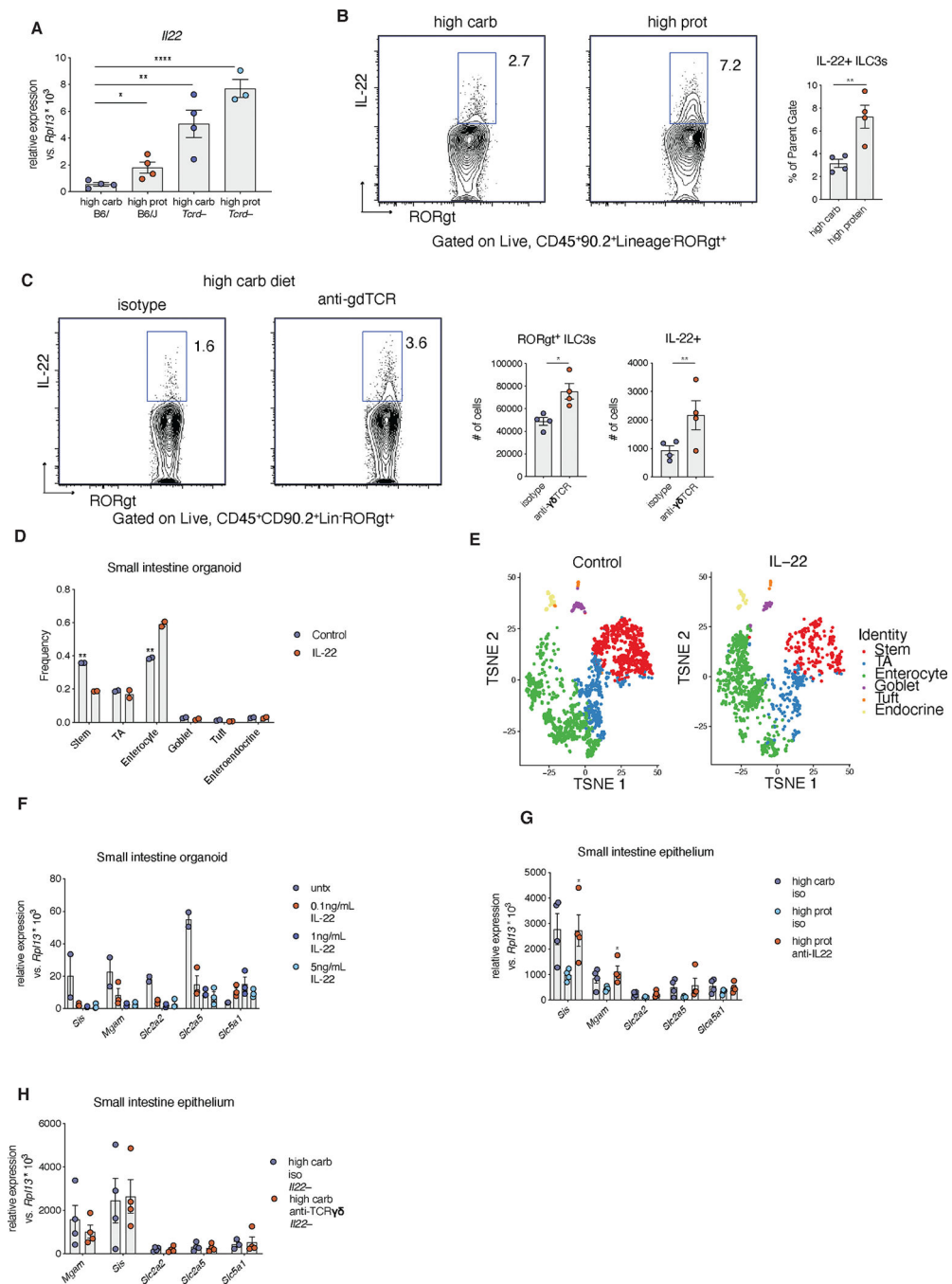
Figure 4. γδ T cells regulate carbohydrate transcriptional program through the suppression of IL-22.

(**A**) *Il22* transcript expression in whole small intestine from wild-type or *Tcrgd*-mice fed high carb or high protein diet (**B**) Representative intracellular cytokine staining and quantification of IL-22 production in small intestine ILC3s from mice fed high-carbohydrate or high-protein diets. (**C**) Representative intracellular cytokine staining (C) and quantification (D) of RORgT expression and IL-22 production in small intestine ILC3s from mice fed high carbohydrate diet and treated with anti-TCRγδ antibody or isotype control.

Frequency **(D)** and t-SNE plots **(E)** showing epithelial subtypes in small intestine organoids treated with IL-22 or control media. **(F)** Expression of carbohydrate transcriptional program in small intestine organoids treated with indicated concentration of IL-22. **(G)** Expression of carbohydrate transcriptional program in small intestine epithelium of mice fed high carbohydrate or high protein diet and treated with anti-IL22 antibody or isotype control. **(H)** Expression of carbohydrate transcriptional program small intestine epithelial cells isolated from IL-22-deficient mice fed high carb diet and treated with anti-TCRγδ antibody or isotype control. n=3–4 mice per group. Data represent mean ± SEM. P-values (except in E) in calculated by Student's t test. P-values in E calculated by Dirichlet-multinomial regression. $*P<0.05$, $**P<0.01$, $***P<0.001$. All data are representative of at least two independent experiments, except D&E, which represent a single sequencing experiment.